Applied Surface Science 615 (2023) 156331

Contents lists available at ScienceDirect

Applied Surface Science

journal homepage: www.elsevier.com/locate/apsusc

Full length article

Molecular mechanisms of pH-tunable stability and surface coverage of polypeptide films

Adam L. Harmat [a,b], Maria Morga [c], Jodie L. Lutkenhaus [d,e], Piotr Batys [c,*], Maria Sammalkorpi [a,b,f,*]

[a] Department of Chemistry and Materials Science, Aalto University, Espoo, P.O. Box 16100, FI-00076 Aalto, Finland
[b] Academy of Finland Center of Excellence in Life-Inspired Hybrid Materials (LIBER), Aalto University, Espoo, P.O. Box 16100, FI-00076 Aalto, Finland
[c] Jerzy Haber Institute of Catalysis and Surface Chemistry, Polish Academy of Sciences, Niezapominajek 8, PL-30239 Krakow, Poland
[d] Artie McFerrin Department of Chemical Engineering, Texas A&M University, College Station, TX 77840, USA
[e] Department of Materials Science and Engineering, Texas A&M University, College Station, TX 77840, USA
[f] Department of Bioproducts and Biosystems, Aalto University, Espoo, P.O. Box 16100, FI-00076 Aalto, Finland

ARTICLE INFO

Keywords:
Poly-L-lysine
Poly-L-arginine
α-quartz
Adsorption mechanism
Hydrogen bonding
Electrostatic interactions

ABSTRACT

Streaming potential and quartz crystal microbalance measurements, combined with all-atom molecular dynamics simulations, were used to study the pH dependency of the adsorption of two basic homopolypeptides, poly-L-lysine (PLL) and poly-L-arginine (PARG), on α-quartz surface. We report that the observed adsorption behavior rises from an interplay of *i*) the change in the number of possible peptide-surface ion pairs between the charged moieties and *ii*) repulsive electrostatic interactions between the polypeptide molecules. For low pH values, polypeptide adsorption was strongest and stable monolayers were formed. However, electrostatic repulsion between the polypeptides led to a relatively low maximum surface coverage. On the other hand, higher pH led to more weakly bound, but significantly denser, peptide films with limited stability. Simulations indicate that electrostatic interactions are the main driving force for adsorption, while hydrogen bonding and non-specific interactions also contribute. Additionally, the important role of the counterions of the negatively charged quartz surface that form a positively charged ion adlayer is highlighted. Ion release of the condensed sodium ions at the charged surface occurs via displacement by polypeptide adsorption. The mechanisms revealed by this work provide systematic guidelines to engineering active surfaces of charged peptides with controlled surface coverage and reversible binding.

1. Introduction

The biocompatible, biodegradable, bioactive and stimuli-responsive behavior of polypeptides (PPs) make them perfect candidates for materials use in biomedical applications [1], such as drug-delivery vehicles [2–4], implantable devices [5,6], or antimicrobial coatings [7]. Even more so, the use of PP materials is gaining interest due to increasing understanding of peptide structure-function relationships and the maturation of recombinant DNA technology, which allows for the synthesis of designed sequence PPs in large yields [1]. For these applications, PP adsorption at solid/liquid interfaces bears significant importance because it is the initial step in self-assembled monolayer (SAM) and multilayered film formation that form the basis of PP materials [8,9]. We focus here on the adsorption of two cationic PPs with mutually different pH responses (i.e. poly-L-lysine (PLL) and poly-L-arginine (PARG)) onto a well-characterized, common pH-responsive substrate, silica α-quartz. Because both the PPs and the substrate are pH-responsive, a variety of adsorption behaviors are to be expected.

The basis for designing PP-based novel materials is their physical and chemical properties and stimuli-responsiveness to environment, see e.g. Refs. [1,10] for reviews. The properties of PPs in bulk solution, such as secondary structure and ionization degree (ID), dictate for example PP self-assembly and adsorption [11,12]. PPs that contain amino acid sequences with ionizable side chain functionalities, such as lysine (Lys) and arginine (Arg), are especially interesting due to their pH-response and salt sensitivity which provide tunable interactions [13–15]. Notably, pH can alter the PP charge state, and electrostatic screening by

* Corresponding authors at: Department of Chemistry and Materials Science, Aalto University, Espoo, P.O. Box 16100, FI-00076 Aalto, Finland (M. Sammalkorpi), Jerzy Haber Institute of Catalysis and Surface Chemistry, Polish Academy of Sciences, Niezapominajek 8, PL-30239 Krakow, Poland (P. Batys).
E-mail addresses: Adam.Harmat@aalto.fi (A.L. Harmat), maria.morga@ikifp.edu.pl (M. Morga), Jodie.Lutkenhaus@tamu.edu (J.L. Lutkenhaus), piotr.batys@ikifp.edu.pl (P. Batys), Maria.Sammalkorpi@aalto.fi (M. Sammalkorpi).

https://doi.org/10.1016/j.apsusc.2023.156331
Received 28 October 2022; Received in revised form 27 December 2022; Accepted 2 January 2023
Available online 4 January 2023

added salt provides a means to control the formation of smart materials based on charged PPs or multifunctional films with incorporated polypeptide chains [14].

PLL ($pK_a \approx 9.85$ [16]) has been studied extensively as a model pH-tunable PP. The secondary structure of PLL is influenced by the protonation state of the chain moieties which can be tailored by the pH of the solution [13,17]. Prior experimental work shows that the secondary structure of PLL changes from α-helix to random coil because of the electrostatic repulsion of the charged side chains as the PP ID, influenced by the pH and pK_a of the PP, increases [13]. The secondary structure can further be influenced by the temperature [18] or peptide chirality [19].

PARG behaves differently due to the relatively high $pK_a \approx 12.1$ [20] of the guanidine group on the amino acid (AA) side chain. Because tuning PARG's ID is limited, PARG remains fully charged and adopts a random coil configuration at all biologically relevant pH values [21–23]. However, a random coil to α-helix transition has been demonstrated using divalent and polyvalent ions [24].

Experimental investigations (e.g. quartz crystal microbalance [25], streaming potential measurements [26] and optical reflectometry [27]) provide information on adsorption phenomenon at the macroscopic scale. For example, the physical and chemical characteristics of the substrate surface, such as density and type of functional groups [28] and surface roughness and morphology [29–31], have been shown to affect PP adsorption. In this work, we focus on silica as the substrate. Besides being pH responsive, silica is also a very well-characterized substrate material [32–38]. Silica is often used as a model substrate in adsorption studies, being e.g. the most common sensor substrate for quartz crystal microbalance with dissipation monitoring measurement technique, but common also in biomedical applications, such as drug delivery systems, biocatalyst supports, or biosensors. These applications rely on biomacromolecule–substrate interactions [34,39–43]. Additionally, silica has been the focus of significant force field development [28,44], increasing the accuracy of computational modeling and via that the attractiveness of silica as a modeling substrate.

Computational modeling allows systematic examination of the adsorption response by enabling precise control of system variables including salt species, ionic strength, and ionization degree. Especially, all-atom molecular dynamics (MD) simulations offer an ideal tool for studying PP adsorption due to the possibility to probe atomic scale interactions, i.e. hydrogen bonding and electrostatic interactions at nanosecond time scales [13,28,45–47]. Prior MD simulations work has highlighted the main mechanism for adsorption of PPs with basic side chain functionalities such as arginine and lysine on silica surfaces. Specifically, electrostatic interactions are major contributors, along with hydrogen bonding between polar groups of the AA side chain and silanol and siloxide groups on the silica surface [27,28,45,47,48]. Adsorption can be modulated by the water solvent structure at the silica surface [46] and the salt species i.e. counterions in the polyelectrolyte-silica system [49]. Quantum chemical methods have indicated that hydrogen bonding between lysine and silanol (SiOH) groups on the silica surface occurs [50,51]. In addition to molecular level modeling, thermodynamics-based and statistical modeling approaches, such as the Random Sequential Adsorption (RSA) model [52,53] and Scaled Particle Theory [54], have been used to gain insight on large-scale features of polypeptide (or other macromolecule) and colloidal adsorption, e.g., maximum surface coverage or adsorption kinetics.

In summary, both experimental and computational studies have demonstrated that the main driving forces of physical adsorption of PPs comprise electrostatic interactions, hydrophobic attraction, and hydrogen bonding [26,28,29,55,55–58]. Mechanisms associated with electrostatic interactions include ion pairing, ion exchange, and cation or anion bridging, see e.g. [28,59,60]. Additionally, ion and solvent release entropy contribute, see e.g. Ref. [61] for review. The aforementioned mechanisms can rise from the electric double layer (EDL) affiliated with the substrate's surface. The structure and dynamics of the EDL are very complex, and therefore, despite over a century of study, significant advances in the field are still made, especially relating to the dynamic nature of the interfacial region, i.e. charging dynamics, non-local charge transfer [62] and phase separation (see recent review [63]). Atomistic detail molecular dynamics with localized charge is a versatile tool used to study the structure of the EDL, especially in regard to polyelectrolyte adsorption, because conventional mean-field models are not able to accurately predict the perturbation caused by the macromolecule on the substrate [64–68]. PP secondary structure type has also been shown to influence adsorption kinetics and the formed monolayer structure [11,27,29,69–71].

The literature survey also reveals that studies systematically mapping the pH dependency of PP adsorption and the interplay of both the substrate and PP charge states remain lacking. Additionally, most adsorption studies in literature have been carried out from concentrated PP suspensions, which despite the greater consumption of the reagents, result in less stable and poorly defined PP layers on the substrate. To fill the gap, we focus here on a model system composed of well-defined homopolypeptides comprising solely of lysine or arginine residues adsorbing on a well-characterized α-quartz silica surface. Both the PPs and the surface change their charge state in response to changes in pH, making the setup ideal for extracting adsorption dependencies on pH. The setup allows systematic charting of the pH dependency in the adsorption and adsorbed film characteristics. Additionally, the use of diluted PP solutions allows precise control of the resulting monolayer, in terms of surface coverage, stability, and viscoelastic properties, as demonstrated by the current work. We combine experimental measurements and MD simulations to extract these dependencies. Experimentally, quartz crystal microbalance method allows study of the polypeptide adsorption, while the streaming potential method enables the determination of the monolayer stability in terms of surface coverage changes during desorption at controlled transport conditions. The use of an α-quartz substrate for streaming potential measurements is not common, adding further value to the work. All-atom detail MD simulations were used to interpret the experimental data, elucidate molecular mechanisms and systematically map the interactions driving the adsorption phenomena. The significance of the work is that the results offer insight into molecular interaction mechanisms responsible for PP adsorption and provide guidelines for the construction of PP layers with tunable adsorption properties and well-defined layer characteristics.

2. Methods

2.1. Experimental materials

Pure crystalline poly-L-lysine hydrobromide, hereafter referred to as PLL, and poly-L-arginine, hereafter referred to as PARG, constitute the two synthetic polypeptides purchased from Sigma Aldrich Merck KGaA, Darmstadt, Germany. The molar mass reported by the manufacturer for the two polypeptides is equal to 150–300 kg mol^{-1} and 15–75 kg mol^{-1}, respectively. The exact molar masses, previously determined using the viscosity method, were equal to 120 kg mol^{-1} and 38 kg mol^{-1} for PLL and PARG, respectively [14,23]. Additionally, the length of PLL and PARG molecules used in this work were determined previously in a wide range of ionic strength. The PLL chain length was 192 nm in pure water and 67 nm in 0.15 M NaCl [14], whereas PARG chain length was 79 nm in water and 36 nm in 0.15 M NaCl [23].

The stock and dilute solutions used in the experiments were prepared by dissolving the proper amount of solid PLL and PARG in NaCl electrolyte. The analytical grade chemicals used for preparing the solutions and investigation of ionic strength-dependent and acid-base properties of the polypeptides, i.e., NaCl, HCl, and NaOH, were purchased from Sigma Aldrich Merck KGaA, Darmstadt, Germany, and Avantor Performance Materials, Poland S.A. The NaCl solutions of a precisely known concentration were prepared using deionized water obtained using Milli-Q Elix & Simplicity 185 purification system from

Millipore SAS Molsheim, France, with the conductivity less than 0.06 μScm^{-1}.

Silicon wafers (Si/α-SiO_2, p-type, boron doped) for examining the adsorption and desorption mechanisms under in-situ conditions using the streaming potential method were purchased from Silchem, Freiberg, Germany. The wafers were cut out to obtain the surface area of 1.0×3.0 cm^2 and thickness 0.1 cm. The pieces of silicon were freshly cleaned before each set of experiments in a 1:1 mixture of H_2SO_4 and H_2O_2 for 30 min, rinsed with Milli-Q water and afterwards immersed in 80 °C Milli-Q water for 30 min. Finally, the silicon pieces were dried in a flow of nitrogen [72,73]. The thickness of the grown SiO_2 layer was measured to be 3.2 ± 0.4 nm [52].

QCM-D silicon/silica quartz crystals (sensors) were AT-cut silica-coated gold crystals characterized by a fundamental shear oscillation frequency of 5 MHz, purchased from QSense, Sweden. The sensors were used in gravimetric measurements using a quartz crystal microbalance with dissipation monitoring (QCM-D). Before each measurement, the QCM-D sensors were immersed in piranha (1:1:1 mixture of H_2SO_4 and H_2O_2, and ultrapure water, prepared 30 minutes before cleaning) for 1.5 min, to obtain the SiO_2 layer. Afterwards, the sensors were rinsed with Milli-Q water and immersed in 80 °C Milli-Q water for 30 min. Finally, the sensors were dried in a flow of nitrogen. The sensors were freshly cleaned before each experiment. The root mean square (rms) roughness of the QCM-D silica sensors, previously examined by AFM conducted in a semicontact mode under ambient conditions, was equal to 0.87 nm [74,75].

2.2. Experimental methods

2.2.1. Electrophoretic mobility and diffusion coefficient measurements

The electrophoretic mobility and diffusion coefficients of PLL and PARG were measured by the combination of electrophoresis with laser Doppler velocimetry (ELDV) and dynamic light scattering (DLS) methods, using a Malvern Zetasizer Nano ZS device.

Unlike diffusion coefficient D, the hydrodynamic diameter d_H is independent of temperature and liquid viscosity which brings an advantage in analyzing suspension stability under various conditions, see in Ref. [76]. The hydrodynamic diameter was calculated using the Stokes–Einstein relationship:

$$d_H = \frac{kT}{3\pi\eta D}, \tag{1}$$

where k is the Boltzmann constant, T is the absolute temperature, and η is the dynamic viscosity of the solution. For polyelectrolyte molecules, the hydrodynamic diameter can be interpreted as the diameter of a sphere with the same hydrodynamic resistance coefficient as the molecule under investigation.

Together, the directly measured d_H and μ_e allow the determination of the zeta potential values of the PPs based on the Henry'os model [77–80]:

$$\zeta_p = \frac{3}{2}\frac{\mu_e\eta}{\varepsilon f(\kappa d_H)}, \tag{2}$$

where $f(\kappa d_H)$ is the correction function [77,78] and κ^{-1} is the double layer thickness.

The electrokinetic charge per single molecule is obtained based on the electrophoretic mobility from the Lorentz–Stokes relationship:

$$q_e = \frac{kT}{D}\mu_e = 3\pi\eta d_H\mu_e. \tag{3}$$

The electrokinetic charge allows one to calculate the number of uncompensated charges N_c responsible for binding the PP molecules to the surface [80–82], i.e. the stability of obtained monolayers:

$$N_c = \frac{q_e}{e}. \tag{4}$$

In this, e is the elementary charge 1.602 × 10^{-19} C. It should be underlined that Eq. (4) is valid for an arbitrary charge distribution, molecular shape, and electrophoretic mobility. However, its accuracy decreases when the double layer thickness does not exceed the hydrodynamic diameter of the molecule.

2.2.2. Streaming potential measurements

The home-made setup that was used for determining the zeta potential of bare and PP-covered surfaces has been described in detail elsewhere [83,84]. In brief, the main part of the measurement cell is a parallel plate channel with dimensions 0.027 × 0.29 × 3.0 cm^3, formed by α-quartz silica surfaces forming the adsorbing walls, separated by a perfluoroethylene spacer. The streaming potential E_s was measured using a pair of Ag/AgCl electrodes as a function of the hydrostatic pressure difference ΔP which causes the flow of an electrolyte through the channel. The overall cell electric conductivity, K_e, was determined using a pair of Pt electrodes. The slope of the E_s vs. ΔP dependence allowed calculating the apparent elektrokinetic potential of a substrate surface (ζ) based on the Smoluchowski relationship:

$$\zeta = \frac{\eta K_e}{\varepsilon}\left(\frac{\Delta E_s}{\Delta P}\right), \tag{5}$$

where η is a dynamic viscosity of the solution, K_e is the specific conductivity of the cell, and ε is the dielectric permittivity.

The procedure of preparing polypeptide monolayers on the α-quartz silica (Si/α-SiO_2) surface was as follows:

i Streaming potential measurements for characterization of bare Si/α-SiO_2 surface under 0.1 M NaCl solution and varying the pH over range 2–12 were performed.

ii Polypeptide monolayers of dense coverage were obtained *in situ* under diffusion-controlled transport. This was realized by filling the electrokinetic cell with a polypeptide (either PLL or PARG) suspension of the concentration of 10 mg L^{-1}, 0.1 M NaCl and a given pH. For each experimental condition, the monolayer was formed over 20 min. The concentration and the time of the monolayer formation were determined on the basis of previous investigations [52,84,85]. Both parameters were sufficient to obtain maximum coverage of the polypeptides on the Si/α-SiO_2 surface.

iii Afterwards, the cell was flushed with a pure electrolyte of the same ionic strength and pH, in order to remove weakly bound polypeptide chains, and the streaming potential of the PP-covered Si/α-SiO_2 surface was measured.

iv In the final step, for the densely packed PP monolayer, desorption experiments were performed in order to determine the influence of pH on the stability of the monolayer. In these experiments, the streaming potential measurements were conducted during rinsing the monolayer with a pure electrolyte of a given pH under the volumetric flow rate equal to 2.1 cm^3 min^{-1}. The time interval of data collection was 15 min at the beginning of the experiment and 40–60 min afterwards, up to 420 minutes.

In the case of bare Si/α-SiO_2, the pH was changed starting from natural pH 5.8 toward the basic pHs. Then, after reaching the pH 12, the pH was changed backward toward acidic pH, up to pH 2.0. The electrokinetic (uncompensated) charge of the surface was calculated using the Gouy–Chapman relationship, valid for symmetric, 1:1 electrolytes:

$$\sigma_0 = \frac{(8\varepsilon kTn_b)^{\frac{1}{2}}}{0.1602}\sinh\frac{e\zeta_i}{2kT}, \tag{6}$$

where σ_0 is the electrokinetic charge density expressed in e nm^{-2} and n_b is the number concentration of ions expressed in m^{-3}.

For a PP-covered surface Eq. (7) allows to convert the zeta potential to PP monolayer coverage [26,86]:

$$\Theta = -\frac{1}{C_i}\ln\frac{\zeta - 0.71\zeta_b}{\zeta_i - 0.71\zeta_b}, \tag{7}$$

where C_i is the dimensionless constant, dependent on the flow damping caused by adsorbed macroions. Assuming side-on adsorption of PPs, C_i is equal to 5.6. [87]. ζ_i is the zeta potential of bare substrate, ζ_b is the bulk zeta potential of the macroion and ζ is the zeta potential obtained from the streaming potential measurements for PP monolayer.

2.2.3. QCM-D measurements

The QCM-D measurements, performed for investigation of adsorption kinetics of both PLL and PARG monolayers, were carried out using a QSenseE1 device (QSense, Gothenburg, Sweden) according to the procedure described in Refs. [75,88,89]. All QCM-D measurements were performed for PP suspensions, at 10 mg L^{-1} concentration, with 0.1 M NaCl electrolyte and for varying pH. In brief, before each measurement, a stable baseline corresponding to pure electrolyte was attained. The flow velocity of pure electrolyte was set to 1.33×10^{-2} cm^3 s^{-1}. Next, the PP suspension was introduced into the thermostated QCM-D cell. The flow velocity of the polypeptide suspension was the same as for the pure electrolyte. The adsorption of the polypeptides was carried out for 25 min. The adsorbed wet mass of PP per unit area, hereafter referred to as the QCM-D mass and denoted by Γ, was calculated from the Sauerbrey equation:

$$\Gamma = -C\frac{\Delta f}{n}, \tag{8}$$

where Γ is wet mass per unit area, Δf is the frequency change, n is the overtone number, and C is the mass sensitivity constant that is dependent on the physical properties of the sensor. For the AT-cut silica-coated gold crystals, C is equal to 0.177 mg m^{-2} Hz [90].

The mass of the adsorbed monolayers was calculated from the frequency changes obtained as the average value from 5 overtones. Simultaneously, using the same overtones, the dissipation was calculated as the average value from 5 overtones (3rd-11th).

2.3. Simulations

All-atom molecular dynamics simulations were carried out using the GROMACS software, version 2020.5 [91]. The AMBER-99SB*-ILDNP [92] force-field was used for the simulations of the PLL and PARG PPs. A recent force-field comparison by Batys et al. [13] reported AMBER99SB*-ILDNP force-field best in capturing the secondary structure response to changes in solution pH. For water, the TIP3P water model as the AMBER compatible water model was employed [93]. AMBER compatible force field parameters for silica α-quartz aqueous interfaces of Emami et al. [44] were used for the silica surface. In prior work, we have successfully used the model for studying adsorption from bio oils [94].

PLL is a weak polyelectrolyte with $pK_a \approx 9.8$ [13,16] while PARG is a relatively strong base with the guanidine side chain functionality $pK_a \approx 12.1$ [20]. Fig. 1(a) shows the chemical structure of the two studied PPs with the ionization states present in the examined pH range. It is worth noting that the pK_a values carry uncertainty as pK_a is dependent on ionic strength, temperature, and the PP chain length (number of AAs) [95]. Additionally, pK_a can change when the PP binds to the substrate [96].

The charge states of the two PPs in the MD simulations were set to match the mean charge state of the PP at a given pH calculated using their respective pK_as and the Henderson–Hasselbalch equation. It is worth noting that recently, constant-pH MD methods have emerged for modeling the changes in the amino acid protonation states caused by pH [97–99]. The approach, however, requires knowing the pKa value for the ionizable group. This depends on the molecular neighborhood, complicating the use for example, for the charged homopolypeptides, such as PLL or PARG. The PPs were generated using Tinker [100]. All studied PPs are 15 AAs long homopolypeptides.

Table 1 summarizes the studied PPs and their AA sequences in terms of charged side chain positioning. The N- and C-termini are capped with acetyl (ACE) and N-methyl amide (NME) groups, respectively. Therefore, only the amino-acid side chain groups are responsible for charge–charge electrostatic interactions. We introduce a notation Lys^+ and Lys (PLL) and Arg^+ and Arg (PARG) to refer to the charged and uncharged amino acids. When present, the charged residues are set at even intervals in the amino acid chain. PARG was only studied as a fully charged Arg^+ chain.

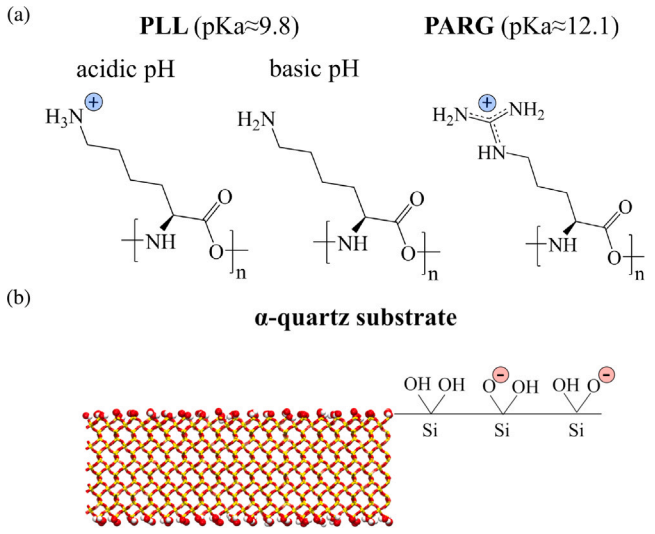

Fig. 1. Chemical structure of a) PLL with charged and neutral side chain and PARG with charged side chain. (b) α-quartz crystal slab used in this work. Oxygen, silicon and hydrogen atoms are red, yellow, and white, respectively. The silanol ≡SiOH and siloxide groups ≡SiO^- are presented on the crystal surface.

The chosen PP chain length in the simulations is long enough to reproduce secondary structure in agreement with circular dichroism spectroscopy experimental results [13]. Additionally, at low ionic strength highly charged PPs can be expected to have negligible finite-size effects from the PP chain length as the electrostatic repulsion causes the peptide end-to-end distance to be linearly dependent on the molar mass [14,23,101].

For PLL, the final 1 μs structures from Batys et al. [13] were used as the secondary structure equilibrated initial configurations for adsorption studies. For PARG, the secondary structure equilibration followed Batys et al. [13] protocol but due to the dominance of the electrostatic interaction in the fully charged PARG chain, 300 ns was enough to equilibrate the secondary structure. Peptide relaxation was performed in water solution with 0.1 M NaCl as added salt and Cl^- ions needed to neutralize the PP charge. Dilute solution conditions were chosen to make comparison between the experimental and modeling work feasible. At higher salt concentrations, the electrode reactions make electrophoretic mobility measurements less feasible.

The α-quartz slab with Q2 surface structure (silanol/siloxide density of 9.4 nm^2) was created using CHARMM-GUI [102]. Four systems with differing IDs, ID = 0 (pH = 3), ID = 0.1 (pH = 6), ID = 0.233 (pH = 10), and ID = 0.3 (pH = 12), were constructed with pH dependency of the ID based on Emami et al. [44]. The size of the xy-periodic crystal slab was $7.37 \times 7.65 \times 2.7$ nm^3 and it was put into a simulation box of $7.37 \times 7.65 \times 10.5$ nm^3. Fig. 1(b) shows the α-quartz slab created and the silanol and siloxide groups on the crystal surface. Charged α-quartz slabs were neutralized by Na^+ counterions, the equilibrated PP was inserted into the simulation box so that its center of mass was 2.3 nm from the plane defined by the surface oxygen atoms of the α-quartz surface, the system was solvated, and the Cl^- counterions of the PP were added. All simulation systems had one PP per α-quartz crystal slab and contained additionally 0.1 M added NaCl. The supplementary information (SI) contains additional information, including Na^+ adlayer equilibration assessment data as Figure S1.

Table 1
Summary of the simulated polypeptides (PPs) and α-quartz surfaces. The PP amino acid sequences, peptide and silica surface ionization degrees (IDs) and corresponding pH are presented. The PP sequences are shown to indicate the positioning of the charged residues in the models.

pH	PP sequence	PP ID	silica ID
PLL			
3.0	ACE-$(Lys^+)_{15}$-NME	1	0
6.0	ACE-$(Lys^+)_{15}$-NME	1	0.1
9.6	ACE-(Lys^+)-Lys-$(Lys^+)_2$-Lys-$(Lys^+)_2$-Lys-$(Lys^+)_2$-Lys-$(Lys^+)_2$-Lys-Lys^+-NME	0.66	0.23
10.2	ACE-Lys-Lys^+-$(Lys)_2$-Lys^+-$(Lys)_2$-Lys^+-$(Lys)_2$-Lys^+-$(Lys)_2$-Lys^+-Lys-NME	0.33	0.23
12.0	ACE-$(Lys)_{15}$-NME	0	0.3
PARG			
3.0	ACE-$(Arg^+)_{15}$-NME	1	0
6.0	ACE-$(Arg^+)_{15}$-NME	1	0.1
10.0	ACE-$(Arg^+)_{15}$-NME	1	0.23

After the initial equilibration of the system, a 50 ns unconstrained NPT simulation was performed. If the PP adsorbed to the α-quartz surface, the production run was continued to 500 ns duration. If the adsorption did not take place within the 50 ns, adsorption tendency was probed by pulling the peptide center of mass z-axially with a rate 2 nm/s toward the surface. Details of the procedure are provided in the SI.

A 20 ns NPT run was performed for three sampling configurations. For PP desorbing in all three runs, adsorption was concluded unlikely but if the PP remained close to the surface, adsorbed for the 20 ns simulation, the production run was continued until a total simulation time of 500 ns was reached. Equilibration was assessed by the root mean square deviation (RMSD) of the PP as a function of simulation time. The last 300 ns were used for the analysis.

The V-rescale thermostat [103] with time constant $\tau_T = 0.1$ ps and reference temperature of 298 K were used. The PP was thermostated separate from water and ions and the α-quartz slab was considered a third thermostatting group. All NPT simulations employ the Parrinello–Rahman barostat [104,105] ($\tau_p = 2$ ps). Anisotropic pressure coupling with compressibilities of 4.5e−6, 4.5e−6 and 4.5e−5 bar^{-1} for x-, y-, and z-directions were used. The x- and y-direction compressibility was assumed to be ten times lower than the compressibility of water to take into account the rigidity of the α-quartz slab. The off-diagonal compressibilities were set to 0 bar^{-1}. The C-H bond vibrations were constrained using the LINCS algorithm [106]. The particle mesh Ewald method [107] was used for long-range electrostatics (cubic interpolation and Fourier spacing set to 0.16). The nonbonded interactions used a 1.0 nm cutoff. The Verlet algorithm with a time step of 2 fs was used for integrating the equations of motion in the production runs.

The adsorption free energy of the PPs was estimated via the potential mean force (PMF) obtained by umbrella sampling. Each umbrella sampling window was sampled for 50 ns in NPT ensemble. For hydrogen bond analysis, standard Gromacs tools were used. For molecular visualizations, VMD [108] was used. Details of the umbrella sampling protocol and performed analyses are provided in the SI.

3. Results and discussion

We first provide results on the experimental determination of bulk PLL and PARG properties that influence PP-PP and PP-surface interactions under varying pH. Next, we focus on characteristics of the bare Si/α-SiO_2 surface that influence PP adsorption at the same conditions. Then, experimental PP adsorption to the surface and characterization of the formed film is examined. For enhanced interpretation, MD simulation results on PP adsorption at varying pH are provided. The presented sequence of data gives a clear view on the influence of single molecule properties on the formation mechanisms and stability of PP films adsorbed to an Si/α-SiO_2 surface.

Bulk solution characteristics of PLL and PARG

Essential bulk characteristics influencing molecule–molecule and molecule–surface interactions include the diffusion coefficient D and the electrophoretic mobility μ_e of PLL and PARG molecules. They were measured simultaneously by DLS and LDV in the same experiment. Eqs. (1) and (2)) provide the dependence of the hydrodynamic diameter and the zeta potential on pH for PLL and PARG molecules (Figs. S2 and S3). Fig. S2 shows that the zeta potential of PLL molecules remains positive in the pH range 3.1–7.2, with an average value of 48 ± 2 mV. At higher pH, the zeta potential monotonically decreases in the pH range 7.8 – 9.5, vanishing at pH above 10.5. This is defined in literature as the isoelectric point [109–111]. Analogously, the zeta potential of PARG molecules remains highly positive in the pH range 3.1 – 8.2, with an average value of 46 ± 2 mV. For higher pH the zeta potential decreases slightly attaining the lowest value of 21 ± 3 mV at pH 12. In contrary to PLL, PARG molecules remain positively charged in the entire examined pH range.

The hydrodynamic diameter of PLL molecules remains constant (d_H = 18 ± 3 nm) in the pH range 3.1–10.5. The d_H value is slightly lower than reported previously for the same molecules but at lower ionic strength [13]. At pH above that range, aggregation is observed, see Fig. S3. In DLS measurements, aggregation shows as higher friction of the molecules, reflected by an increased value of the hydrodynamic diameter. The electrophoretic mobility data is consistent with the DLS investigation. In total, the behavior can be associated with vanishing repulsive electrostatic interactions between the molecules (lower number of uncompensated charges per molecule). Analogously, PARG's hydrodynamic diameter remains practically independent of pH (up to pH 12), with a value of 8 ± 1 nm. This suggests that only slight changes in the molecule conformation take place.

The physicochemical parameters, comprised of the diffusion coefficients, the corresponding hydrodynamic diameters, the electrophoretic mobility and the corresponding zeta potentials, as well as the number of uncompensated charges per molecule, for the examined pH range 3–12 are gathered in Table 2.

Surface characteristics

An important factor for the interpretation of PP adsorption is the zeta potential of the bare Si/α-SiO_2 surface (ζ_i), which was determined by streaming potential measurements. The dependence of ζ_i on pH for 0.1 M NaCl, calculated from Eq. (5), is shown in Fig. S4. The zeta potential of the bare Si/α-SiO_2 surface remains negative for the entire studied pH range. For pH 9–12, $\zeta_i = -52 \pm 5$ mV. Approaching acidic conditions, an increase in the zeta potential was observed, with $\zeta_i = -32$ mV and −10 mV measured for pHs 5.8 and 3.1, respectively. The isoelectric point of the Si/α-SiO_2 surface was determined to be pH 2.5, in agreement with the literature [112–114].

Moreover, using the measured zeta potential values and applying Eq. (6), the corresponding electrokinetic (uncompensated) charge of the

Table 2
Summary of physicochemical characteristics of PLL and PARG measured experimentally at various pH. Diffusion coefficient D, hydrodynamic diameter d_H, electrophoretic mobility μ_e, zeta potential ζ_b, and number of uncompensated charges N_c per PLL or PARG molecule are presented. $T = 298$ K and $I = 0.1$ M NaCl in all measurements. The conditions modeled by the MD simulations are marked with gray background.

pH	$D \times 10^{-11}$ [m^2 s^{-1}]	d_H [nm]	μ_e [mm cm (V s)$^{-1}$]	ζ_b [mV]	N_c
PLL					
3.1 ± 0.1	2.7	18.0 ± 5	2.6 ± 0.2	49 ± 3	28
3.6 ± 0.1	2.9	16.7 ± 3	2.5 ± 0.1	47 ± 2	25
4.5 ± 0.1	3.1	15.7 ± 2	2.4 ± 0.1	46 ± 6	23
5.8 ± 0.1	3.1	16.0 ± 4	2.6 ± 0.2	49 ± 4	25
7.6 ± 0.1	2.7	18.0 ± 4	2.2 ± 0.1	43 ± 2	23
9.5 ± 0.1	3.1	16.0 ± 2	1.7 ± 0.3	26 ± 4	16
10.5 ± 0.1	3.3	15.0 ± 2	0.4 ± 0.2	8 ± 4	4
12.0 ± 0.1	2.6	19.0 ± 6	−0.7 ± 0.1	−12 ± 2	8
PARG					
3.1 ± 0.1	6.4	7.7 ± 2	2.4 ± 0.2	44 ± 3	11
5.1 ± 0.1	5.5	8.9 ± 3	2.5 ± 0.1	47 ± 2	13
5.9 ± 0.1	5.8	8.5 ± 2	2.4 ± 0.1	45 ± 2	13
7.4 ± 0.1	6.6	8.3 ± 2	2.5 ± 0.2	48 ± 3	12
8.5 ± 0.1	5.5	8.9 ± 2	2.4 ± 0.1	45 ± 2	13
10.0 ± 0.1	6.2	7.9 ± 2	1.9 ± 0.3	36 ± 4	9
11.9 ± 0.1	6.4	7.7 ± 2	1.2 ± 0.2	21 ± 3	6

surface σ_0 was determined to vary between −0.0454e nm^{-2} for pH 3.1 and −0.3055e nm^{-2} for pH 12. The determined surface properties of the Si/α-SiO_2 at varying pH values are collected in Table 3.

Table 3
The Si/α-SiO_2 physicochemical characteristics summary. Values for the zeta potential (ζ_i), measured via streaming potential method, and the electrokinetic surface charge (σ_0), calculated from the Gouy–Chapman Eq. (6), at various pH. $T = 298$ K and $I = 0.1$ NaCl. The conditions modeled by the MD simulations are marked with gray background.

pH	ζ_i [mV]	σ_0 [e nm^{-2}]
2.2	5 ± 10	0.0226
3.1	−10 ± 4	−0.0454
4.2	−20 ± 4	−0.0925
5.8	−32 ± 8	−0.1816
7.7	−40 ± 3	−0.1991
8.9	−48 ± 4	−0.2493
9.6	−52 ± 4	−0.2766
10.2	−52 ± 8	−0.2765
12.0	−56 ± 8	−0.3055

pH-dependent adsorption response

Streaming potential and QCM-d measurements

For PP adsorption, the QCM-D method was employed, allowing for monitoring real-time changes in adsorbed PP film mass, and therefore the surface coverage. Fig. 2 shows representative QCM-D data for PLL and PARG adsorption at various pH conditions and constant ionic strength (0.1 M NaCl). For both PLL and PARG, saturation of adsorbed mass, revealed by the plateau region at longer measurement times, was observed at all investigated pHs. This indicates that the formed monolayer no longer grows in mass with increasing deposition time. A higher total adsorbed mass indicates that the adsorbed layer covers the surface more densely.

For PLL, see Fig. 2(a), QCM-D determined the highest adsorbed mass to be at pH 11.0, then 10.5, 9.5, 12, 6.0, and finally 3.0. The determined adsorbed mass of the monolayer does not correlate directly neither with the PLL effective charge nor substrate charge, see Tables 2 and 3. For example, at pH 3.2 where the adsorbed mass is the lowest, the Si/α-SiO_2 surface is only slightly charged but the PLL is highly and oppositely charged. Furthermore, at pH 6.2, where a relatively low adsorbed mass was observed, both PLL and Si/α-SiO_2 surface are highly charged. This could be related with priorly reported side-on orientation of adsorbed PLL molecules [52], combined with the strong electrostatic repulsion between them rising from the high charge. In agreement with this deduction, when the PLL effective charge decreases, at pH 9.5 and 10.2, the surface coverage significantly increases, with pH 10.5 leading to the highest surface coverage by the PLL monolayer.

At pH 12, PLL is almost neutral in its charge and the Si/α-SiO_2 surface is highly charged. Seemingly counterintuitively, under these conditions, significant adsorption occurred. One explanation for this could be that the PLL molecules slowly aggregate in these conditions, and the aggregates deposit on the surface. However, this adsorption mechanism would show in the adsorption kinetics, i.e. the initial region of the adsorption curve in Fig. 2(a). As the adsorption kinetics appear similar to the data curves corresponding to the other pH values, we consider this explanation unlikely. Another possible explanation is that

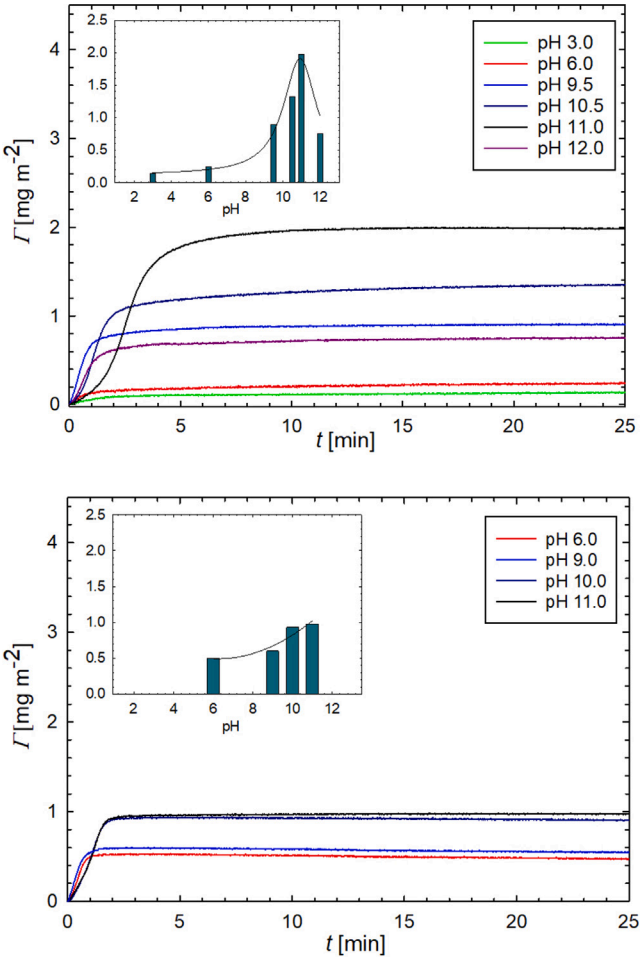

Fig. 2. QCM-D data showing changes in adsorbed mass Γ of (a) PLL and (b) PARG on Si/α-SiO_2 substrate at various pH and 0.1 M NaCl. The insets show the mass adsorbed after 25 min as a function of pH.

the highly charged surface induces a shift in the PLL pK_a, i.e. protonation. Such shifts in pK_a for weak polyelectrolytes have been observed during the complex formation [115].

Similarly for PARG, the highest adsorbed mass was observed also at higher pH, i.e., pH 10.0 and 11.0, followed by pH 9.0 and 6.0, see Fig. 2(b). As before, the charging of the surface and the PP do not directly explain the response. At pH 6.0, where the adsorbed mass is the lowest, the Si/α-SiO_2 substrate is only slightly charged. Little increase in adsorbed mass is observed for pH 9.0, where the charge of PARG molecules is similar to one calculated for pH 6.0 and only the increase in the absolute value of the surface charge is observed. The

increase in the adsorbed mass is observed for pH 10 and 11 where the surface charge increases in absolute value, whereas the charge of PARG molecules decreases.

This behavior can be explained by the effect of the silica substrate whose negative charge increases with pH. The presence of the charged substrate decreases the repulsion between adsorbing PARG chains. This promotes adsorption, which is explicitly seen comparing the results obtained for pH 6–9 and 10–11. This effect was described and quantitatively interpreted in terms of attractive three-body interactions for PAMAM dendrimers [90].

The pH-related response of PARG adsorption, i.e., the higher surface coverage at higher pH, is similar to the PLL adsorption response. As PARG remains fully charged in the examined pH range, this suggests that the behavior described for PLL could be universal for linear molecules of this size with similar surface and molecule charging response to pH changes.

The changes in dissipation at various pH values, see Fig. S5, allow for a qualitative discussion of the film's structure. The lowest dissipation occurs for pH 6, which suggests the side-on orientation of the adsorbed molecules. At this pH, the PPs are fully charged and can adsorb on the substrate to form a thin and well-attached monolayer, which was previously observed in Ref. [26]. At lower and higher pH values, the changes in the dissipation are much higher, indicating that the film is thicker and softer than the case of pH 6. For a value of pH 3, the end-on orientation of the PP can attributed to the low surface charge density of the substrate, (i.e., only few adsorption sites are available for a single PP chain). Similar end-on adsorption has been reported for fibrinogen, see Ref. [116]. On the other hand, at higher pH values, the PP is less charged, and the number of contacts with the substrate is therefore limited. Also, at higher pH values, one can observe changes in the PP secondary structures, as indicated by previous circular dichroism studies, see Refs. [13,23]. This results in more compact PP structures.

To examine the adsorption of PP in more detail, the binding of the PPs and the coverage of the PP monolayer on the surface after the adsorption and during the rinsing process was determined *in situ* by direct streaming potential measurements. Eq. (7) allows for determination of the dimensionless coverage of the polypeptide monolayer based on the zeta potential at each step of the rinsing experiment of the streaming potential measurement (Fig. S6), the zeta potential of the macromolecules in bulk (Table 2), and the Si/α-SiO_2 substrate zeta potential (Table 3), respectively. The resulting coverage vs the desorption time is shown in Fig. 3.

The data of Fig. 3(a) show that the PLL monolayers undergo desorption at all examined pHs. Rinsing with pure electrolyte of a given pH leads to loss in initial coverage. After 420 min of rinsing at pH 3.0 or 6.0, 50% of the initial PLL coverage had desorbed. For higher pHs, significantly greater loss was observed, with desorption reaching 80% and 90% of the initial coverage at pH 9.5 and 10.5, respectively. At pH 12.0, due to the very low effective charge of PLL, the streaming potential measurements were unfeasible. Analogous results are obtained for PARG. Fig. 3(b) shows that PARG monolayers also undergo desorption at all examined pHs. Specifically, 420 min of rinsing at pH 6.0 led to desorption of 60% of the initial coverage. Desorption reached c.a. 80% of the initial coverage at pH 10.0. This can result from the higher effective charge of PARG at higher pH, in comparison to the PLL.

Jointly, the surface coverages, determined via QCM-D, and desorption behavior, determined from streaming potential measurements, allow conclusions regarding the general features of the adsorbed PP monolayers at various pH. At pH close to 7, which corresponds to highly charged PPs, the adsorption is very strong which leads to a stable monolayer. However, at these conditions, the maximum surface coverage remains limited due to electrostatic repulsion of the PPs. In consequence, the highest packing density is obtained at a pH in which the PPs are slightly less charged. Even though electrostatic binding of the PP to the oppositely charged surface becomes weaker by this,

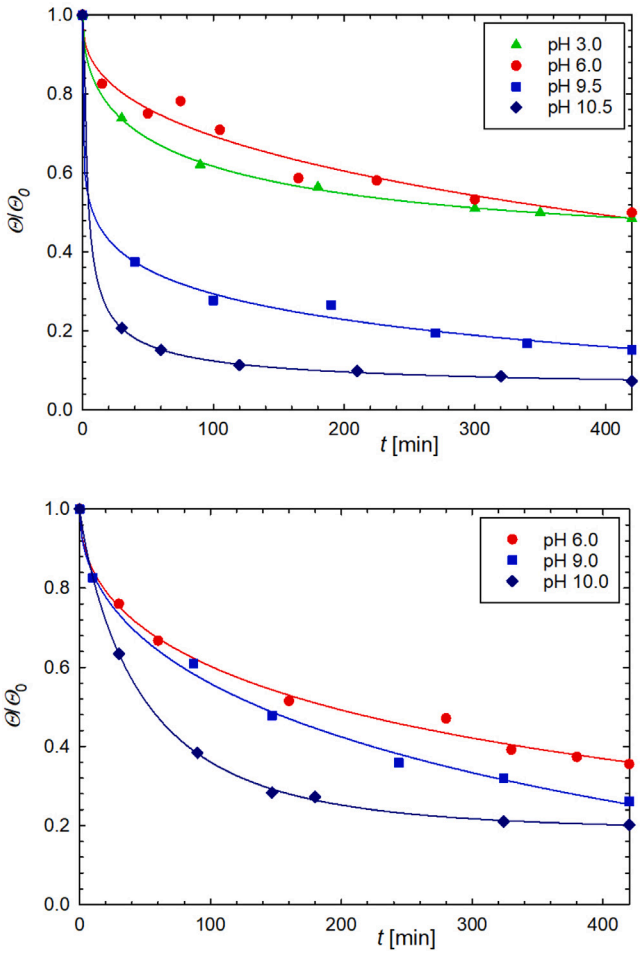

Fig. 3. Dependence of the normalized surface coverage (Θ/Θ_0) of (a) PLL and (b) PARG monolayer on the desorption time t at varying pH. The coverage is determined from streaming potential measurements via Eq. (7). The initial (at $t = 0$ min) coverage Θ_0 is used as the normalization coverage. Solid lines provide a guide to the eye. All data corresponds to $I = 0.1$ M NaCl, measured at $T = 298$ K. The measured zeta potential values are provided in the SI, Fig. S6.

the decreased PP-PP electrostatic repulsion allows for a higher packing density. However, the result is a less stable monolayer, i.e., desorption is faster. Consistent with the observations here, it is worth mentioning that PLL monolayers with higher packing density can also be obtained by increasing the ionic strength [52].

Molecular simulations and the interaction mechanisms of PP adsorption

MD simulations of the corresponding PLL, PARG, and the Si/α-SiO_2 surface charge states at a selected set of pH conditions (marked in gray in Tables 2 and 3) were performed to obtain insight into the molecular mechanisms of PP adsorption. The results of PP adsorption simulations are summarized in Figs. 4 and 5. In the simulations, the effect of pH is represented by changing the fraction of charged AAs in the peptides or silanol vs siloxide groups at the α-quartz surface, as captured by the ionization degree.

Fig. 4(a) summarizes the PLL adsorption results of the MD simulations. In the MD simulations, the 15 monomer PLL oligomers did not adsorb at conditions corresponding to pH 3.0 or 12.0, but readily adsorbed at charge states corresponding to pH 6.0, 9.6 and 10.2; however, the latter pH case was successful only after guiding the adsorption energy landscape via initially pulling the peptide toward the surface, see SI for precise protocol. Adsorption free energy was estimated via umbrella sampling: the ΔG_{ads} values in Fig. 4(b) indicate

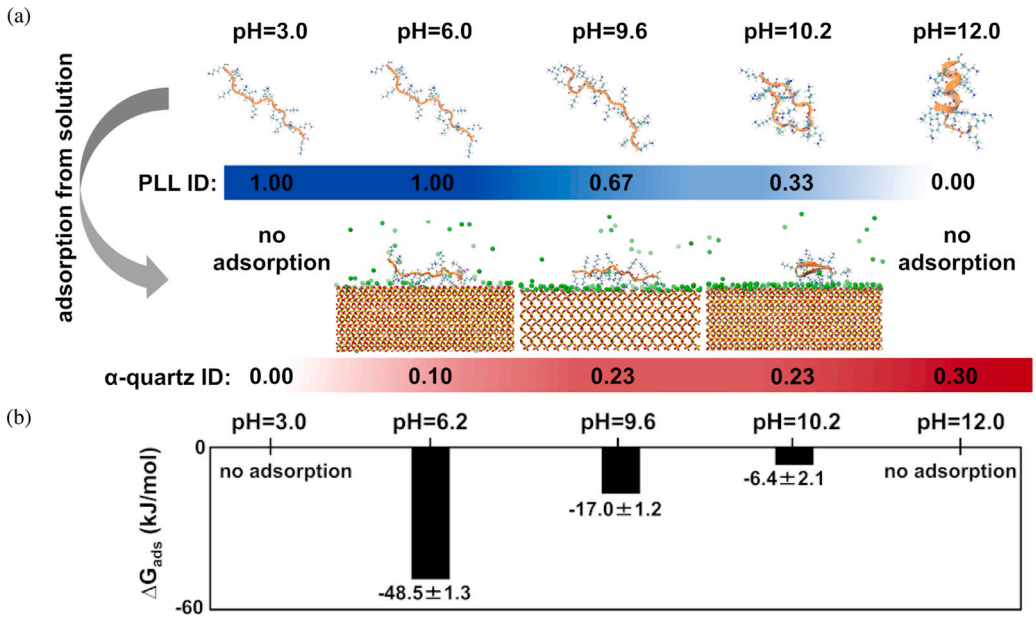

Fig. 4. Molecular simulations results summary of PLL adsorption at conditions corresponding to different pH values. a) Representative simulation snapshots of PLL molecular conformations in bulk solution and as adsorbed on the surface. Color bars show the negative charge of the α-quartz surface and the positive charge of the PLL by ionization degree ID in blue and red, respectively. ID is calculated as the fraction of charged groups in the PLL and at the α-quartz surface. In the visualizations, the green beads show the sodium ions but water molecules and chloride ions are omitted for clarity. b) The corresponding adsorption free energies ΔG_{ads} estimated by umbrella sampling PMF calculations. The error is estimated by bootstrapping based standard deviation.

strong adsorption at pH 6.2 and decreasing adsorption strength with increasing pH.

Fig. 5(a) is the corresponding summary of the PARG adsorption results in the simulations. PARG adsorbed in the simulations at conditions corresponding to pH 6.0 and 10.0 but at conditions corresponding to pH 3.0, PARG desorbed even after guiding the adsorption pathway by pulling the PP toward the surface. The adsorption free energy estimates in Fig. 5(b) show a decrease in adsorption strength with increasing pH despite the increasing α-quartz surface charge. Consistent with the ΔG_{ads}, also the root mean square fluctuations of PARG at conditions corresponding to pH 10.0 indicate decreased surface binding stability, see SI Figure S7.

The decrease in adsorption free energies observed in MD simulations with increasing pH explains well the lower stability of experimentally formed monolayers at higher pH (see Fig. 3 for the corresponding streaming potential data). Also, the MD modeling suggests that PARG should interact with the substrate more strongly than PLL, which is in line with other experimental studies comparing the binding strength of lysine and arginine [117]. It should be noted, however, that in this work different molar mass of PARG and PLL is used in the experiments, while the same PP length corresponding to short oligomers is used in the MD simulations. Therefore the desorption experiments of PLL and PARG cannot be directly compared with each other.

Simulations allow for analysis of the adsorption mechanisms at the molecular level. Both the PLL and PARG simulations results directly suggest that the adsorption is driven by attractive electrostatic interactions between the positively charged AAs and the negatively charged α-quartz surface (≡SiO$^-$ groups), as expected. The conditions where adsorption took place correspond to those where PLL and PARG AA residues were positively charged and the α-quartz surface negatively charged by siloxide groups (≡SiO$^-$). Notably at pH 3.0, the α-quartz surface is neutral (ID = 0), and both PLL and PARG desorb in the simulations. The case of PLL at pH 12.0 is discussed below.

The results also suggest that, besides direct PP-surface electrostatic attraction driving adsorption, the Na^+ ions have a role in PP adsorption by forming an adlayer on the α-quartz. Fig. 6 shows the cumulative number count of Na^+ ions vs distance from the substrate at varying pH. The data are calculated based on a radial distribution function

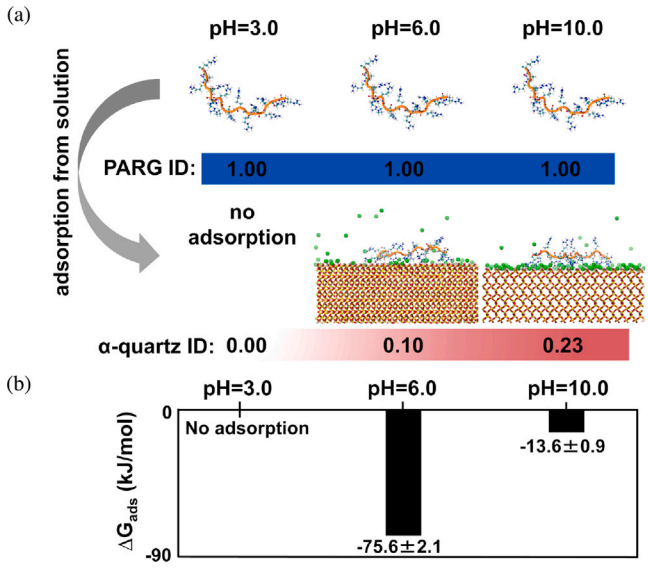

Fig. 5. Molecular simulations results summary of PARG adsorption at conditions corresponding to different pH values. a) Representative simulation snapshots of PARG molecular conformations in bulk solution and as adsorbed on the surface. Color bars show the negative charge of the α-quartz surface and the positive charge of the PLL by ionization degree ID in blue and red, respectively. ID is calculated as the fraction of charged groups in the PARG and at the α-quartz surface. In the visualizations, the green beads show the sodium ions but water molecules and chloride ions are omitted for clarity. b) The corresponding adsorption free energies ΔG_{ads} estimated by umbrella sampling PMF calculations. The error is estimated by bootstrapping based standard deviation.

determined between the oxygen atoms on the crystal surface and the Na^+ ions. The Na^+ ion adsorption curves are shifted to the right with PP adsorption. This implies that the number of Na^+ ions on the α-quartz surface decreases when PLL or PARG adsorbs. Because PLL and PARG carry positive charge at the conditions where adsorption was observed, the results suggest that the adsorption between the Na^+

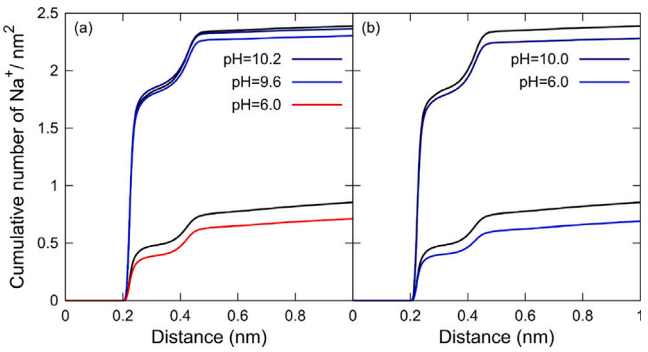

Fig. 6. Cumulative number count of sodium ions per α-quartz surface area vs distance for a) PLL and b) PARG at varying pH conditions. The data is calculated based on radial distribution function between the oxygen atom on the α-quartz surface and the sodium ions. For each pH value, the data corresponding to Na^+ ions both with the PP adsorbed (colored curves) and without the PP in the simulation setup (black curves) are presented. For the simulation setup, an approximation that the α-quartz ionization degree remains same at pH 9.6 and 10.2 has been made.

ions and the positively charged PPs is competitive, see Fig. 7. Peptide binding releases the ions to the solution. In the simulations data, this shows also in the strong decrease of ΔG_{ads} values at higher pH where more Na^+ ions are on the α-quartz surface, see Figs. 4(b) and 5(b). Support for the observations is provided by the desorption kinetics of PARG (see Fig. 3(b)): the slope decreases faster with increasing pH. Both experimental and computational data show that the EDL structure on the α-quartz substrate surface, altered by the surface charge and resulting change in Na^+ ion density, affects PP film stability and density.

In addition to long-range electrostatic interactions, shorter range localized attractions such as hydrogen bonding can contribute to adsorption. Fig. S8 presents the hydrogen bonds per AA residue for the PPs in the simulations. Hydrogen bonding between the PP and the surface becomes an evident contributor to adsorption at pH values where the charge difference between the PP and the α-quartz surface is minor or not present. The data show that PARG can form the largest number of hydrogen bonds per AA residue. This is because all three nitrogen atoms of the guanidine group of the arginine side chain can act as hydrogen bond donors [118].

The experimental and MD simulations data align well, supporting the electrostatically driven adsorption behavior. However, some discrepancy exists for the adsorption of PLL at extreme values of pH, (i.e. conditions corresponding to pH 3.0 and 12.0, where adsorption is observed experimentally but simulations do not predict adsorption). There are several possible reasons for this. In the simulation setup, the conditions assigned to correspond to pH 3.0 assume that the α-quartz surface has zero total charge; however, in experiments, the zeta potential at this pH is slightly negative (see Table 3). Thus, although the modeling setup refers to "pH 3.0", the modeled conditions correspond more to the experimental surface charge observed for pH below 2.5. At the other extreme pH of 12.0, the highly charged surface can induce a shift in the pK_a of PLL, thus altering the protonation state. The employed simulation model assumes a constant protonation state, and therefore the performed modeling cannot capture such shifts in pK_a. The modeling considers the PP with the most likely ID and even, regularly spaced charge distribution as the best representation model for a specific pH. The approach is naturally a simplification that is not taking into account the presence of multitude of PPs with dynamically changing, mutually differing IDs and charge distributions in the experiments. Additionally, the modeling considers one PP molecule per simulation, therefore omitting PP-PP interactions in the adsorption response. It is worth noting that PP-PP interactions can alter both the IDs and the dynamics of adsorption through structural reorganization of the PP film during consecutive PP adsorption. However, the simplifications in

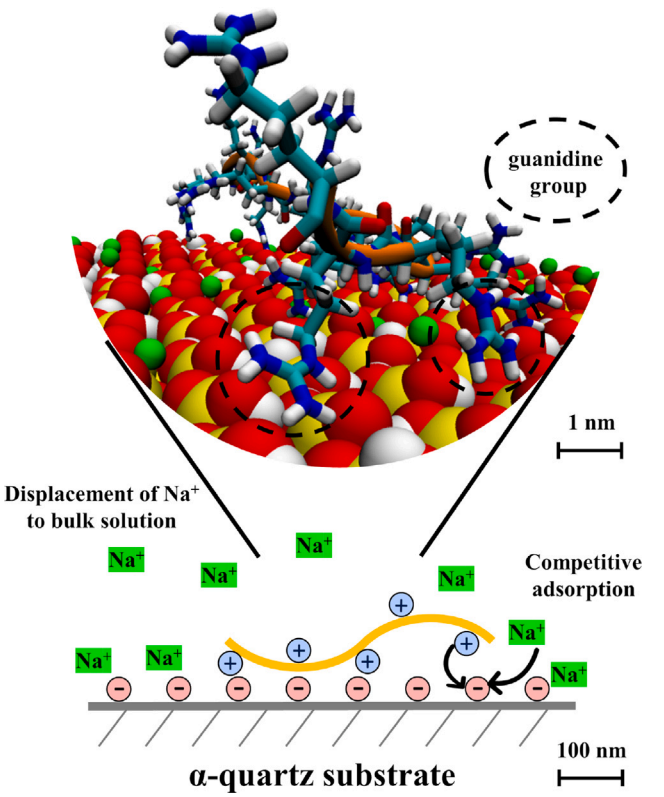

Fig. 7. Schematic illustration of competitive adsorption between the PP and Na^+ ions on α-quartz surface and MD simulation snapshot of PARG at pH = 10.0. The atomistic detail level model highlights the ion exchange mechanism with no Na^+ ions in the close vicinity of guanidine groups that are interacting with the surface.

the modeling of this work allow extracting the basic dependencies and are set to capturing the interaction mechanisms between the PP and α-quartz surface.

Further limitations of the modeling efforts result from the use of empirical force field and localized point charges which disregard electronic polarization and charge redistribution effects. Previous works have discussed the resulting overbinding of ions in MD simulations and suggested improvements in the form of a polarizable force field, see e.g. Refs. [119–121]. Electrostatics in adsorption can be enhanced because of this, especially in conditions differing from bulk aqueous solution [122]. The silica force field developed by Emami et al. [44] used in this work has addressed the issue by rigorous parameterization and comparison with experimental data, such as zeta potential of the silica surface. The experimental validation demonstrates good performance of the model in regards to α-quartz interfacial properties, such as Na^+ ion binding, that play a fundamental role in PP adsorption.

Finite-size affects, i.e. short PPs in the simulations, can also affect simulation prediction. However, in systems with relatively low ionic strength and highly charged PPs such as herein, PP chain length effects should be negligible as the electrostatic repulsion causes the peptide end-to-end distance to be linearly dependent on the molar mass [14]. However, PPs with low ionization degree are likely to fold onto themselves as longer chains, and this cannot be observed with the short segments studied by the MD simulations here. Additionally, MD simulations results of PPs are highly affected by the employed force-field [13], and the force-field choice here was carefully based on prior experimental validation on the PP secondary structure vs pH [13].

4. Conclusions

The effect of pH on PLL and PARG adsorption on a silica surface was investigated experimentally via streaming potential and QCM-D

methods, complemented by MD simulations. As polypeptide monolayers are often applied as functional coatings, the possibility to control their surface coverage and adsorption stability is especially important. In this work, we showed how pH can be used as a means to control PP monolayer surface coverage and adsorption stability. The molecular interaction mechanisms responsible for the macroscopic film properties and pH response were probed by combining experiments with all-atom molecular dynamics.

At pH close to neutral, stable PP monolayers with relatively low surface coverage formed. At higher pH, the monolayers formed were highly packed and desorbed more easily. At moderate pH, i.e., close to 9, the adsorbed monolayer had both surface coverage and stability to a reasonable degree. Interestingly, a similar response was observed for both PLL and PARG, which suggests that the mechanism could be universal for PP layer formation between oppositely charged PPs and surfaces. The MD simulations of the corresponding systems showed that adsorption of both PLL and PARG is mainly driven by electrostatic interactions between the positively charged PPs and the negative α-quartz surface, while hydrogen bonding was also demonstrated. The MD simulations predicted competitive adsorption of PLL and PARG with Na^+ ions. Analysis of the simulation data showed that Na^+ ions are displaced to the bulk solution when the positively charged PPs adsorb. This indicates an ion exchange mechanism. Both MD simulations and the streaming potential measurements highlight that PP film adsorption stability is influenced by the Na^+ ions in the adlayer on the α-quartz surface.

We conclude that the observed adsorption behavior rises from the interplay of *i*) the change in the number of possible PP-surface ion pairs and *ii*) repulsive electrostatic interactions between the PP molecules. In total, the trends for pH-sensitive adsorption for PLL and PARG align well with similar studies on weak and strong polyelectrolyte adsorption on charged surfaces [123–125]. The adsorption mechanism predicted by the atomistic detail MD simulations in this work have been previously demonstrated experimentally for similar systems of polyelectrolyte [126,127] and protein adsorption [128–130]. Notably, the theoretical modeling work of Evers et al. [123] suggests that a maxima in adsorbed polyelectrolyte arises when electrostatic interactions dominate and a low contribution of non-electrostatic interactions to the free energy is present — in agreement with the current work. Summarizing, our work provides a systematic characterization of charged PP adsorption to an oppositely charged surface and demonstrates how experiments and MD simulations can be used jointly as a highly valuable combination in extracting molecular level guidelines in terms of interactions and bottom-up tuning of molecular systems for materials design.

CRediT authorship contribution statement

Adam L. Harmat: Visualization, Investigation, Formal analysis, Writing – original draft. **Maria Morga:** Conceptualization, Visualization, Investigation, Formal analysis, Writing – original draft, Writing – reviewing and editing. **Jodie L. Lutkenhaus:** Writing – reviewing and editing. **Piotr Batys:** Conceptualization, Supervision, Funding acquisition, Resources, Writing – original draft, Writing – reviewing and editing. **Maria Sammalkorpi:** Conceptualization, Supervision, Funding acquisition, Resources, Writing – reviewing and editing.

Declaration of competing interest

The authors declare that they have no known competing financial interests or personal relationships that could have appeared to influence the work reported in this paper.

Data availability

Data associated with the simulations of the manuscript is available at https://doi.org/10.23729/86b3e079-25b4-450f-84a9-3260f26cb18c. Other data will be made available on request.

Acknowledgments

This work was supported by the Academy of Finland through its Centres of Excellence Programme (2022–2029, LIBER) under project no. 346111 (M.S.), Business Finland Co-Innovation grant No. 3767/31/2019 (M.S.), the National Science Centre, Poland (grant no. 2018/31/D/ST5/01866) (P.B. and M.M.), and the U.S. National Science Foundation, grant No. 1905732 (J.L.). We are grateful for the support by FinnCERES Materials Bioeconomy Ecosystem. Computational resources by CSC IT Centre for Finland, PLGrid Infrastructure (Poland), and RAMI – RawMatters Finland Infrastructure are also gratefully acknowledged.

Appendix A. Supplementary data

Supplementary material related to this article can be found online at https://doi.org/10.1016/j.apsusc.2023.156331.

References

[1] D. Chow, M.L. Nunalee, D.W. Lim, A.J. Simnick, A. Chilkoti, Peptide–based biopolymers in biomedicine and biotechnology, Mater. Sci. Eng. R Rep. 62 (4) (2008) 125–155.
[2] J. Habault, J.-L. Poyet, Recent advances in cell penetrating peptide-based anticancer therapies, Molecules 24 (5) (2019).
[3] K. Szczepanowicz, U. Bazylińska, J. Pietkiewicz, L. Szyk-Warszyńska, K.A. Wilk, P. Warszyński, Biocompatible long-sustained release oil-core polyelectrolyte nanocarriers: from controlling physical state and stability to biological impact, Adv. Colloid Interface Sci. 222 (2015) 678–691.
[4] S. Łukasiewicz, K. Szczepanowicz, K. Podgórna, E. Błasiak, N. Majeed, S.O. Ogren, W. Nowak, P. Warszyński, M. Dziedzicka-Wasylewska, Encapsulation of clozapine in polymeric nanocapsules and its biological effects, Colloids Surf. B 140 (2016) 342–352.
[5] J. Borges, J.F. Mano, Molecular interactions driving the layer-by-layer assembly of multilayers, Chem. Rev. 114 (18) (2014) 8883–8942.
[6] H. Knopf-Marques, J. Barthes, S. Lachaal, A. Mutschler, C. Muller, F. Dufour, M. Rabineau, E.-J. Courtial, J. Bystroňová, C. Marquette, P. Lavalle, N.E. Vrana, Multifunctional polymeric implant coatings based on gelatin, hyaluronic acid derivative and chain length-controlled poly(arginine), Mater. Sci. Eng. C 104 (2019) 109898.
[7] F. Boulmedais, B. Frisch, O. Etienne, P. Lavalle, C. Picart, J. Ogier, J.-C. Voegel, P. Schaaf, C. Egles, Polyelectrolyte multilayer films with pegylated polypeptides as a new type of anti-microbial protection for biomaterials, Biomaterials 25 (11) (2004) 2003–2011.
[8] E. Gatto, M. Venanzi, Self-assembled monolayers formed by helical peptide building blocks: A new tool for bioinspired nanotechnology, Polym. J. 45 (2013) 468–480.
[9] D.T. Haynie, L. Zhang, J.S. Rudra, W. Zhao, Y. Zhong, N. Palath, Polypeptide multilayer films, Biomacromolecules 6 (6) (2005) 2895–2913.
[10] J. Huang, A. Heise, Stimuli responsive synthetic polypeptides derived from N-carboxyanhydride (NCA) polymerisation, Chem. Soc. Rev. 42 (2013) 7373–7390.
[11] M. Binazadeh, A. Faghihnejad, L.D. Unsworth, H. Zeng, Understanding the effect of secondary structure on molecular interactions of poly-L-lysine with different substrates by SFA, Biomacromolecules 14 (10) (2013) 3498–3508.
[12] A. Ghosh, M. Haverick, K. Stump, X. Yang, M.F. Tweedle, J.E. Goldberger, Fine-tuning the pH trigger of self-assembly, J. Am. Chem. Soc. 134 (8) (2012) 3647–3650.
[13] P. Batys, M. Morga, P. Bonarek, M. Sammalkorpi, pH-induced changes in polypeptide conformation: force-field comparison with experimental validation, J. Phys. Chem. B 124 (14) (2020) 2961–2972.
[14] Z. Adamczyk, M. Morga, D. Kosior, P. Batys, Conformations of poly-L-lysine molecules in electrolyte solutions: modeling and experimental measurements, J. Phys. Chem. C 122 (40) (2018) 23180–23190.
[15] C.N. Pace, G.R. Grimsley, J.M. Scholtz, Protein ionizable groups: p*K* values and their contribution to protein stability and solubility, J. Biol. Chem. 284 (20) (2009) 13285–13289.
[16] A. Dos, V. Schimming, S. Tosoni, H.-H. Limbach, Acid–base interactions and secondary structures of poly-L-lysine probed by 15N and 13C solid state NMR and Ab initio model calculations, J. Phys. Chem. B 112 (49) (2008) 15604–15615.
[17] Y.P. Myer, The pH-induced helix-coil transition of poly-L-lysine and poly-L-glutamic acid and the 238-mμ dichroic band, Macromolecules 2 (6) (1969) 624–628.
[18] J.-S. Chiou, T. Tatara, S. Sawamura, Y. Kaminoh, H. Kamaya, A. Shibata, I. Ueda, The α-helix to β-sheet transition in poly(L-lysine): effects of anesthetics and high pressure, Biochim. Biophys. Acta 1119 (2) (1992) 211–217.

[19] S.L. Perry, L. Leon, K.Q. Hoffmann, M.J. Kade, D. Priftis, K.A. Black, D. Wong, R.A. Klein, C.F. Pierce, 3rd, K.O. Margossian, J.K. Whitmer, J. Qin, J.J. de Pablo, M. Tirrell, Chirality-selected phase behaviour in ionic polypeptide complexes, Nature Commun. 6 (1) (2015) 6052.

[20] C. Dharmayanti, T.A. Gillam, M. Klingler-Hoffmann, H. Albrecht, A. Blencowe, Strategies for the development of pH-responsive synthetic polypeptides and polymer-peptide hybrids: recent advancements, Polymers 13 (4) (2021).

[21] E. Eiríksdóttir, K. Konate, Ü. Langel, G. Divita, S. Deshayes, Secondary structure of cell-penetrating peptides controls membrane interaction and insertion, Biochim. Biophys. Acta Biomemb. 1798 (6) (2010) 1119–1128.

[22] T. Hayakawa, Y. Kondo, H. Yamamoto, Secondary structure of poly-L-arginine and its derivatives, Bull. Chem. Soc. Jpn. 42 (7) (1969) 1937–1941.

[23] M. Morga, P. Batys, D. Kosior, P. Bonarek, Z. Adamczyk, Poly-L-arginine molecule properties in simple electrolytes: molecular dynamic modeling and experiments, Int. J. Environ. Res. Public Health 19 (6) (2022) 3588.

[24] S. Ichimura, K. Mita, M. Zama, Conformation of poly(L-arginine). I. Effects of anions, Biopolymers 17 (12) (1978) 2769–2782.

[25] M. Porus, P. Maroni, M. Borkovec, Response of adsorbed polyelectrolyte monolayers to changes in solution composition, Langmuir 28 (50) (2012) 17506–17516.

[26] M. Morga, Z. Adamczyk, D. Kosior, M. Kujda-Kruk, Kinetics of poly-L-lysine adsorption on mica and stability of formed monolayers: theoretical and experimental studies, Langmuir 35 (37) (2019) 12042–12052.

[27] M. Jiang, I. Popa, P. Maroni, M. Borkovec, Adsorption of poly(L-lysine) on silica probed by optical reflectometry, Colloids Surf. A Physicochem. Eng. Asp. 360 (1) (2010) 20–25.

[28] S.V. Patwardhan, F.S. Emami, R.J. Berry, S.E. Jones, R.R. Naik, O. Deschaume, H. Heinz, C.C. Perry, Chemistry of aqueous silica nanoparticle surfaces and the mechanism of selective peptide adsorption, J. Am. Chem. Soc. 134 (14) (2012) 6244–6256.

[29] J.-H. Choi, S.-O. Kim, E. Linardy, E.C. Dreaden, V.P. Zhdanov, P.T. Hammond, N.-J. Cho, Influence of pH and surface chemistry on poly(L-lysine) adsorption onto solid supports investigated by quartz crystal microbalance with dissipation monitoring, J. Phys. Chem. B 119 (33) (2015) 10554–10565.

[30] R. Notman, T.R. Walsh, Molecular dynamics studies of the interactions of water and amino acid analogues with quartz surfaces, Langmuir 25 (3) (2009) 1638–1644.

[31] L.B. Wright, T.R. Walsh, Facet selectivity of binding on quartz surfaces: free energy calculations of amino-acid analogue adsorption, J. Phys. Chem. C 116 (4) (2012) 2933–2945.

[32] P. Eugene, Adsorption on Silica Surfaces, Dekker, New York, United States, 2000.

[33] A.P. Legrand, The Surface Properties of Silicas, Wiley, New York, United States, 1998.

[34] A. Rimola, D. Costa, M. Sodupe, J.-F. Lambert, P. Ugliengo, Silica surface features and their role in the adsorption of biomolecules: computational modeling and experiments, Chem. Rev. 113 (6) (2013) 4216–4313.

[35] G.H. Bolt, Determination of the charge density of silica sols, J. Phys. Chem. 61 (9) (1957) 1166–1169.

[36] J. Sonnefeld, Determination of surface charge density constants for spherical silica particles using a linear transformation, J. Colloid Interface Sci. 183 (2) (1996) 597–599.

[37] T. Tadros, J. Lyklema, Adsorption of potential-determining ions at the silica-aqueous electrolyte interface and the role of some cations, J. Electroanal. Chem. Interfacial Electrochem. 17 (3) (1968) 267–275.

[38] R. Zerrouk, A. Foissy, R. Mercier, Y. Chevallier, J.-C. Morawski, Study of Ca^{2+}-induced silica coagulation by small angle scattering, J. Colloid Interface Sci. 139 (1) (1990) 20–29.

[39] S.A. Mackowiak, A. Schmidt, V. Weiss, C. Argyo, C. von Schirnding, T. Bein, C. Bräuchle, Targeted drug delivery in cancer cells with red-light photoactivated mesoporous silica nanoparticles, Nano Lett. 13 (6) (2013) 2576–2583.

[40] M.W. Ambrogio, C.R. Thomas, Y.-L. Zhao, J.I. Zink, J.F. Stoddart, Mechanized silica nanoparticles: a new frontier in theranostic nanomedicine, Acc. of Chem. Res. 44 (10) (2011) 903–913.

[41] C. Sanchez, B. Julián, P. Belleville, M. Popall, Applications of hybrid organic–inorganic nanocomposites, J. Mater. Chem. 15 (2005) 3559–3592.

[42] A. Popat, S.B. Hartono, F. Stahr, J. Liu, S.Z. Qiao, G. Qing (Max) Lu, Mesoporous silica nanoparticles for bioadsorption, enzyme immobilisation, and delivery carriers, Nanoscale 3 (2011) 2801–2818.

[43] M. Hartmann, Ordered mesoporous materials for bioadsorption and biocatalysis, Chem. Mater. 17 (18) (2005) 4577–4593.

[44] F.S. Emami, V. Puddu, R.J. Berry, V. Varshney, S.V. Patwardhan, C.C. Perry, H. Heinz, Force field and a surface model database for silica to simulate interfacial properties in atomic resolution, Chem. Mater. 26 (8) (2014) 2647–2658.

[45] M. Nonella, S. Seeger, Monitoring peptide-surface interaction by means of molecular dynamics simulation, Chem. Phys. 378 (1) (2010) 73–81.

[46] J. Schneider, L. Colombi Ciacchi, Specific material recognition by small peptides mediated by the interfacial solvent structure, J. Am. Chem. Soc. 134 (4) (2012) 2407–2413.

[47] F.S. Emami, V. Puddu, R.J. Berry, V. Varshney, S.V. Patwardhan, C.C. Perry, H. Heinz, Prediction of specific biomolecule adsorption on silica surfaces as a function of pH and particle size, Chem. Mater. 26 (19) (2014) 5725–5734.

[48] H. Chen, X. Su, K.-G. Neoh, W.-S. Choe, QCM-D analysis of binding mechanism of phage particles displaying a constrained heptapeptide with specific affinity to SiO_2 and TiO_2, Anal. Chem. 78 (14) (2006) 4872–4879.

[49] G.R. Quezada, R.E. Rozas, P.G. Toledo, Polyacrylamide adsorption on (101) quartz surfaces in saltwater for a range of pH values by molecular dynamics simulations, Miner. Eng. 162 (2021) 106741.

[50] A. Rimola, M. Sodupe, P. Ugliengo, Affinity scale for the interaction of amino acids with silica surfaces, J. Phys. Chem. C 113 (14) (2009) 5741–5750.

[51] J.W. Han, J.N. James, D.S. Sholl, First principles calculations of methylamine and methanol adsorption on hydroxylated quartz (0001), Surf. Sci. 602 (14) (2008) 2478–2485.

[52] D. Kosior, M. Morga, P. Maroni, M. Cieśla, Z. Adamczyk, Formation of poly-L-lysine monolayers on silica: modeling and experimental studies, J. Phys. Chem. A 124 (8) (2020) 4571–4581.

[53] P. Kubala, P. Batys, J. Barbasz, P. Weroński, M. Cieśla, Random sequential adsorption: An efficient tool for investigating the deposition of macromolecules and colloidal particles, Adv. Colloid Interface Sci. 306 (2022) 102692.

[54] M. Vuorte, S. Kuitunen, P.R. Van Tassel, M. Sammalkorpi, Equilibrium state model for surfactants in oils: Colloidal assembly and adsorption, J. Colloid Interface Sci. 630 (2023) 783–794.

[55] V. Puddu, C.C. Perry, Peptide adsorption on silica nanoparticles: evidence of hydrophobic interactions, ACS Nano 6 (7) (2012) 6356–6363.

[56] D. Horinek, A. Serr, M. Geisler, T. Pirzer, U. Slotta, S.Q. Lud, J.A. Garrido, T. Scheibel, T. Hugel, R.R. Netz, Peptide adsorption on a hydrophobic surface results from an interplay of solvation, surface, and intrapeptide forces, Proc. Natl. Acad. Sci. USA 105 (8) (2008) 2842–2847.

[57] J. Queiroz, C. Tomaz, J. Cabral, Hydrophobic interaction chromatography of proteins, J. Biotechnol. 87 (2) (2001) 143–159.

[58] W. Norde, Driving forces for protein adsorption at solid surfaces, Macromol. Symp. 103 (1) (1996) 5–18.

[59] S. Wang, J. Lin, P. Huang, Advances on the use of biodegradable proteins/peptides in photothermal theranostics, J. Nanomater. 2016 (2016) 1–10.

[60] M.A. Khedkar, S.R. Satpute, S.B. Bankar, P.V. Chavan, Adsorptive removal of unsaturated fatty acids using ion exchange resins, J. Chem. Eng. Data 66 (1) (2021) 308–321.

[61] D. Harries, S. May, A. Ben-Shaul, Counterion release in membrane–biopolymer interactions, Soft Matter 9 (2013) 9268–9284.

[62] Y. Zhang, J. Tang, Z. Ni, Y. Zhao, F. Jia, Q. Luo, L. Mao, Z. Zhu, F. Wang, Real-time characterization of the fine structure and dynamics of an electrical double layer at electrode–electrolyte interfaces, J. Phys. Chem. 12 (22) (2021) 5279–5285.

[63] J. Wu, Understanding the electric double-layer structure, capacitance, and charging dynamics, Chem. Rev. 122 (12) (2022) 10821–10859.

[64] B.M. Lowe, Y. Maekawa, Y. Shibuta, T. Sakata, C.-K. Skylaris, N.G. Green, Dynamic behaviour of the silica-water-bio electrical double layer in the presence of a divalent electrolyte, Phys. Chem. Chem. Phys. 19 (2017) 2687–2701.

[65] B.M. Lowe, C.-K. Skylaris, N.G. Green, Y. Shibuta, T. Sakata, Molecular dynamics simulation of potentiometric sensor response: the effect of biomolecules, surface morphology and surface charge, Nanoscale 10 (2018) 8650–8666.

[66] Y. Maekawa, Y. Shibuta, T. Sakata, Distinctive potential behavior at the oxidized surface of a semiconductor device in a concentrated aqueous salt solution, Chem. Electro. Chem. 1 (9) (2014) 1516–1524.

[67] Y. Maekawa, Y. Shibuta, T. Sakata, Effect of double-stranded DNA on electrical double layer structure at oxide/electrolyte interface in classical molecular dynamics simulation, Chem. Phys. Lett. 619 (2015) 152–157.

[68] S. Dewan, V. Carnevale, A. Bankura, A. Eftekhari-Bafrooei, G. Fiorin, M.L. Klein, E. Borguet, Structure of water at charged interfaces: a molecular dynamics study, Langmuir 30 (27) (2014) 8056–8065.

[69] T. Cosgrove, J. Fergie-Woods, On the kinetics and reversibility of polymer adsorption, Colloids Surf. 25 (1) (1987) 91–99.

[70] E. Pefferkorn, A. Haouam, R. Varoqui, Kinetics of exchange between adsorbed and free polymers at a solid/liquid interface, Macromolecules 22 (6) (1989) 2677–2682.

[71] S. Grohmann, H. Rothe, K. Liefeith, Investigations on the secondary structure of polypeptide chains in polyelectrolyte multilayers and their effect on the adhesion and spreading of osteoblasts, Biointerphases 7 (1) (2012) 62.

[72] C. Schinke, P. Christian Peest, J. Schmidt, R. Brendel, K. Bothe, M.R. Vogt, I. Kröger, S. Winter, A. Schirmacher, S. Lim, H.T. Nguyen, D. MacDonald, Uncertainty analysis for the coefficient of band-to-band absorption of crystalline silicon, AIP Adv. 5 (6) (2015) 067168.

[73] I.H. Malitson, Interspecimen comparison of the refractive index of fused silica, J. Opt. Soc. Amer. 55 (10) (1965) 1205–1209.

[74] M. Wasilewska, Z. Adamczyk, A. Pomorska, M. Nattich-Rak, M. Sadowska, Human serum albumin adsorption kinetics on silica: influence of protein solution stability, Langmuir 35 (7) (2019) 2639–2648.

[75] A. Michna, A. Pomorska, M. Nattich-Rak, M. Wasilewska, Z. Adamczyk, Hydrodynamic solvation of poly(amido amine) dendrimer monolayers on silica, J. Phys. Chem. C 124 (32) (2020) 17684–17695.

[76] M. Oćwieja, M. Morga, Z. Adamczyk, Self-assembled silver nanoparticles monolayers on mica-AFM, SEM, and electrokinetic characteristics, J. Nanopart. Res. 15 (3) (2013) 1460.

[77] R.J. Hunter, Applications of the zeta potential, in: R.J. Hunter (Ed.), Zeta Potential in Colloid Science, Academic Press, 1981, pp. 219–257, (Chapter 6).

[78] A. Delgado, F. González-Caballero, R. Hunter, L. Koopal, J. Lyklema, Measurement and interpretation of electrokinetic phenomena, J. Colloid Interface Sci. 309 (2) (2007) 194–224.

[79] R.W. O'Brien, R.J. Hunter, The electrophoretic mobility of large colloidal particles, Can. J. Chem. 59 (13) (1981) 1878–1887.

[80] M. Morga, Z. Adamczyk, D. Kosior, Silica monolayer formation and stability determined by in situ streaming potential measurements, Electrochim. Acta 206 (2016) 409–418.

[81] M. Morga, Z. Adamczyk, D. Kosior, Silica nanoparticle monolayers on a macroion modified surface: formation mechanism and stability, Phys. Chem. Chem. Phys. 19 (2017) 22721–22732.

[82] M. Morga, A. Michna, Z. Adamczyk, Formation and stability of polyelectrolyte/polypeptide monolayers determined by electrokinetic measurements, Colloids Surf. A: Physicochem. Eng. Asp. 529 (2017) 302–310.

[83] M. Zembala, Z. Adamczyk, Measurements of streaming potential for mica covered by colloid particles, Langmuir 16 (4) (2000) 1593–1601.

[84] M. Morga, Z. Adamczyk, Monolayers of cationic polyelectrolytes on mica – Electrokinetic studies, J. Colloid Interface Sci. 407 (2013) 196–204.

[85] M. Morga, Z. Adamczyk, S. Gödrich, M. Oćwieja, G. Papastavrou, Monolayers of poly-l-lysine on mica – Electrokinetic characteristics, J. Colloid Interface Sci. 456 (2015) 116–124.

[86] K. Sadlej, E. Wajnryb, J. Bławzdziewicz, M.L. Ekiel-Jeżewska, Z. Adamczyk, Streaming current and streaming potential for particle covered surfaces: Virial expansion and simulations, J. Chem. Phys. 130 (14) (2009) 144706.

[87] Z. Adamczyk, K. Sadlej, E. Wajnryb, M. Nattich, M. Ekiel-Jeżewska, J. Bławzdziewicz, Streaming potential studies of colloid, polyelectrolyte and protein deposition, Adv. Colloid Interface Sci. 153 (1) (2010) 1–29.

[88] J. Maciejewska-Prończuk, M. Morga, Z. Adamczyk, M. Oćwieja, M. Zimowska, Homogeneous gold nanoparticle monolayers—QCM and electrokinetic characteristics, Colloids Surf. A Physicochem. Eng. Asp. 514 (2017) 226–235.

[89] A. Michna, P. Batys, M. Morga, A. Pomorska, M. Wytrwal-Sarna, M. Kepczynski, Z. Adamczyk, Formation of strong polycation (poly[(3-allylamino-2-hydroxypropyl)trimethylammonium chloride]) monolayers on mica, silica, and gold substrates: modeling and experimental studies, J. Phys. Chem. C 123 (31) (2019) 19022–19032.

[90] B.P. Cahill, G. Papastavrou, G.J.M. Koper, M. Borkovec, Adsorption of poly(amido amine) (PAMAM) dendrimers on silica: importance of electrostatic three-body attraction, Langmuir 24 (2) (2008) 465–473.

[91] M.J. Abraham, T. Murtola, R. Schulz, S. Páll, J.C. Smith, B. Hess, E. Lindahl, GROMACS: high performance molecular simulations through multi-level parallelism from laptops to supercomputers, SoftwareX 1–2 (2015) 19–25.

[92] A.E. Aliev, M. Kulke, H.S. Khaneja, V. Chudasama, T.D. Sheppard, R.M. Lanigan, Motional timescale predictions by molecular dynamics simulations: case study using proline and hydroxyproline sidechain dynamics, Proteins 82 (2) (2014) 195–215.

[93] W.L. Jorgensen, J. Chandrasekhar, J.D. Madura, R.W. Impey, M.L. Klein, Comparison of simple potential functions for simulating liquid water, J. Phys. Chem. 79 (2) (1983) 926–935.

[94] M. Vuorte, S. Vierros, S. Kuitunen, M. Sammalkorpi, Adsorption of impurities in vegetable oil: a molecular modelling study, J. Colloid Interface Sci. 571 (2020) 55–65.

[95] J. Reijenga, A. van Hoof, A. van Loon, B. Teunissen, Development of methods for the determination of pK_a values, Anal. Chem. Insights 8 (2013) 53–71.

[96] J.L. Lutkenhaus, K. McEnnis, P.T. Hammond, Nano- and microporous layer-by-layer assemblies containing linear poly(ethylenimine) and poly(acrylic acid), Macromolecules 41 (16) (2008) 6047–6054.

[97] P. Dobrev, S.P.B. Vemulapalli, N. Nath, C. Griesinger, H. Grubmüller, Probing the accuracy of explicit solvent constant pH molecular dynamics simulations for peptides, J. Chem. Theory Comput. 16 (4) (2020) 2561–2569.

[98] P. Buslaev, N. Aho, A. Jansen, P. Bauer, B. Hess, G. Groenhof, Best practices in constant pH MD simulations: accuracy and sampling, J. Chem. Theory Comput. 18 (10) (2022) 6134–6147.

[99] N. Aho, P. Buslaev, A. Jansen, P. Bauer, G. Groenhof, B. Hess, Scalable constant pH molecular dynamics in GROMACS, J. Chem. Theory Comput. 18 (10) (2022) 6148–6160.

[100] J.A. Rackers, Z. Wang, C. Lu, M.L. Laury, L. Lagardère, M.J. Schnieders, J.-P. Piquemal, P. Ren, J.W. Ponder, Tinker 8: software tools for molecular design, J. Chem. Theory Comput. 14 (10) (2018) 5273–5289.

[101] Z. Adamczyk, P. Batys, W. Płaziński, M. Morga, D. Lupa, A. Michna, Macroion molecule properties from slender body hydrodynamics, Polym. Adv. Technol. 32 (10) (2021) 3900–3908.

[102] S. Jo, T. Kim, V.G. Iyer, W. Im, CHARMM-GUI: a web-based graphical user interface for CHARMM, J. Comput. Chem. 29 (11) (2008) 1859–1865.

[103] G. Bussi, D. Donadio, M. Parrinello, Canonical sampling through velocity rescaling, J. Chem. Phys. 126 (1) (2007) 014101.

[104] M. Parrinello, A. Rahman, Polymorphic transitions in single crystals: a new molecular dynamics method, J. Appl. Phys. 52 (12) (1981) 7182–7190.

[105] M. Parrinello, A. Rahman, P. Vashishta, Structural transitions in superionic conductors, Phys. Rev. Lett. 50 (1983) 1073–1076.

[106] B. Hess, H. Bekker, H.J.C. Berendsen, J.G.E.M. Fraaije, LINCS: a linear constraint solver for molecular simulations, J. Comput. Chem. 18 (12) (1997) 1463–1472.

[107] U. Essmann, L. Perera, M.L. Berkowitz, T. Darden, H. Lee, L.G. Pedersen, A smooth particle mesh ewald method, J. Chem. Phys. 103 (19) (1995) 8577–8593.

[108] W. Humphrey, A. Dalke, K. Schulten, VMD: visual molecular dynamics, J. Mol. Graph. 14 (1) (1996) 33–38.

[109] C. Picart, P. Lavalle, P. Hubert, F.J.G. Cuisinier, G. Decher, P. Schaaf, J.-C. Voegel, Buildup mechanism for poly(l-lysine)/hyaluronic acid films onto a solid surface, Langmuir 17 (23) (2001) 7414–7424.

[110] S.E. Burke, C.J. Barrett, pH-responsive properties of multilayered poly(l-lysine)/hyaluronic acid surfaces, Biomacromolecules 4 (6) (2003) 1773–1783.

[111] L. Richert, Y. Arntz, P. Schaaf, J.-C. Voegel, C. Picart, pH dependent growth of poly(L-lysine)/poly(L-glutamic) acid multilayer films and their cell adhesion properties, Surf. Sci. 570 (1) (2004) 13–29.

[112] H. Michael, D. Williams, Electrochemical properties of quartz, J. Electroanal. Chem. Interfacial Elecetrochem. 179 (1) (1984) 131–139.

[113] G.R. Wiese, R.O. James, T.W. Healy, Discreteness of charge and solvation effects in cation adsorption at the oxide/water interface, Discuss. Faraday Soc. 52 (1971) 302–311.

[114] R.O. James, G.A. Parks, Characterization of aqueous colloids by their electrical double-layer and intrinsic surface chemical properties, in: E. Matijević (Ed.), Surface and Colloid Science, Springer US, Boston, MA, 1982, pp. 119–216.

[115] J. Choi, M.F. Rubner, Influence of the degree of ionization on weak polyelectrolyte multilayer assembly, Macromolecules 38 (1) (2005) 116–124.

[116] M. Wasilewska, Z. Adamczyk, M. Sadowska, F. Boulmedais, M. Cieśla, Mechanisms of fibrinogen adsorption on silica sensors at various pHs: experiments and theoretical modeling, Langmuir 35 (35) (2019) 11275–11284.

[117] V. Petrauskas, E. Maximowitsch, D. Matulis, Thermodynamics of ion pair formations between charged poly(amino acid)s, J. Phys. Chem. B 119 (37) (2015) 12164–12171.

[118] C.W. Reiss, Y. Xiong, S.A. Strobel, Structural basis for ligand binding to the guanidine-I riboswitch, Structure 25 (1) (2017) 195–202.

[119] D.A. Tolmachev, O.S. Boyko, N.V. Lukasheva, H. Martinez-Seara, M. Karttunen, Overbinding and qualitative and quantitative changes caused by simple Na^+ and K^+ ions in polyelectrolyte simulations: comparison of force fields with and without NBFIX and ECC corrections, J. Chem. Theory Comput. 16 (1) (2020) 677–687.

[120] I.V. Leontyev, A.A. Stuchebrukhov, Electronic continuum model for molecular dynamics simulations, J. Chem. Phys. 130 (8) (2009) 085102.

[121] A. Catte, M. Girych, M. Javanainen, C. Loison, J. Melcr, M.S. Miettinen, L. Monticelli, J. Määttä, V.S. Oganesyan, O.H.S. Ollila, J. Tynkkynen, S. Vilov, Molecular electrometer and binding of cations to phospholipid bilayers, Phys. Chem. Chem. Phys. 18 (2016) 32560–32569.

[122] M. Vuorte, S. Kuitunen, M. Sammalkorpi, Physisorption of bio oil nitrogen compounds onto montmorillonite, Phys. Chem. Chem. Phys. 23 (2021) 21840–21851.

[123] O. Evers, G. Fleer, J. Scheutjens, J. Lyklema, Adsorption of weak polyelectrolytes from aqueous solution, J. Colloid Interface Sci. 111 (2) (1986) 446–454.

[124] N.G. Hoogeveen, M.A. Cohen Stuart, G.J. Fleer, Polyelectrolyte adsorption on oxides: I. Kinetics and adsorbed amounts, J. Colloid Interface Sci. 182 (1) (1996) 133–145.

[125] J. Blaakmeer, M.R. Bohmer, M.A. Cohen Stuart, G.J. Fleer, Adsorption of weak polyelectrolytes on highly charged surfaces. Poly(acrylic acid) on polystyrene latex with strong cationic groups, Macromolecules 23 (8) (1990) 2301–2309.

[126] M. Balastre, J. Persello, A. Foissy, J.-F. Argillier, Binding and ion-exchange analysis in the process of adsorption of anionic polyelectrolytes on barium sulfate, J. Colloid Interface Sci. 219 (1) (1999) 155–162.

[127] J. de Reese, J. Plank, Adsorption of polyelectrolytes on calcium carbonate – which thermodynamic parameters are driving this process? J. Am. Ceram. Soc. 94 (10) (2011) 3515–3522.

[128] W. Norde, J. Lyklema, The adsorption of human plasma albumin and bovine pancreas ribonuclease at negatively charged polystyrene surfaces: V. Microcalorimetry, J. Colloid Interface Sci. 66 (2) (1978) 295–302.

[129] J. Andrade, V. Hlady, Protein adsorption and materials biocompatibility: a tutorial review and suggested hypotheses, biopolymers/non-exclusion HPLC, Adv. Polym. Sci. 79 (1986) 1–63.

[130] Z. Adamczyk, Protein adsorption: A quest for a universal mechanism, Curr. Opin. Colloid Interface Sci. 41 (2019) 50–65.